

Accurate estimation of prediction models for operator-induced defects in assembly manufacturing processes

*Original*

Accurate estimation of prediction models for operator-induced defects in assembly manufacturing processes / Galetto, M.; Verna, E.; Genta, G.. - In: QUALITY ENGINEERING. - ISSN 0898-2112. - 32:4(2020), pp. 595-613. [10.1080/08982112.2019.1700274]

*Availability:*

This version is available at: 11583/2808834 since: 2020-10-19T11:42:57Z

*Publisher:*

Taylor and Francis Inc.

*Published*

DOI:10.1080/08982112.2019.1700274

*Terms of use:*

This article is made available under terms and conditions as specified in the corresponding bibliographic description in the repository

*Publisher copyright*

Taylor and Francis postprint/Author's Accepted Manuscript

This is an Accepted Manuscript of an article published by Taylor & Francis in QUALITY ENGINEERING on 2020, available at <http://www.tandfonline.com/10.1080/08982112.2019.1700274>

(Article begins on next page)

ARTICLE

Open Access

# High-efficiency multi-scale holographic volumetric 3D printing with a phase light modulator

Maria Isabel Álvarez-Castaño<sup>1✉</sup>, Riccardo Rizzo<sup>1</sup>, Viola Sgarminato<sup>1,2</sup>, Ye Pu<sup>1</sup> and Christophe Moser<sup>1✉</sup>

## Abstract

Light-based 3D printing with photocurable resins enables the rapid fabrication of complex structures with high resolution and fidelity. Tomographic Volumetric Additive Manufacturing (TVAM) employs a digital micromirror device (DMD) to project amplitude light patterns into rotating resin volumes, producing 3D geometries through photopolymerization. Typically, the light projection efficiency in such binary amplitude modulator-based systems is below a few percent. Recent advancements introduced phase encoding in TVAM using binary amplitude modulators and the Lee Hologram method, increasing axial control and boosting light efficiency to about 10%. In this work, we present the first 3D printing platform utilizing a phase light modulator (PLM), based on an array of micro-electromechanical piston mirrors. Compared to amplitude encoding, phase encoding with the PLM yields a 70-fold increase in laser power efficiency. By coupling this efficient light engine with a speckle reduction method in holographic volumetric additive manufacturing (HoloVAM), we experimentally demonstrate printing 3D objects across different scales from hundreds of micrometers to centimeters and with various materials from acrylate-based resins to soft hydrogels, including cell-laden hydrogels with a concentration of 1 million cells per mL. Micro-CT revealed a  $\sim 30.3 \mu\text{m}$  as the smallest positive feature printed. Moreover, we introduce the use of gelatin Thiol/Norbornene as a material for printing with the Holographic VAM technique, which allows us to print large-scale objects (up to  $3 \times 3 \times 4 \text{ cm}^3$ ) within 2 minutes using only a 150 mW laser diode. The PLM opens up new avenues in volumetric AM for holographic techniques using low-cost single-mode laser diodes.

## Introduction

Three-dimensional (3D) Additive Manufacturing (AM), better known as 3D printing, has been a breakthrough in many fields such as tissue engineering<sup>1</sup>, regenerative medicine<sup>2</sup>, aerospace<sup>3</sup>, optical components, and many others. The first modern 3D printing method was light-based proposed by Kodama in 1981<sup>4</sup> which consisted of selectively solidifying material point-by-point or layer-by-layer to build three-dimensional objects. Since then, various AM methods have been developed<sup>5–8</sup> using different materials. Layerless 3D technologies do not rely on layer-by-layer deposition. Such technologies are referred to as Volumetric Additive Manufacturing (VAM). Recently,

several light-based VAM methods working with single-photon absorption have been developed. In reverse tomography, known as tomographic volumetric additive manufacturing (TVAM)<sup>9,10</sup>, an entire three-dimensional object is simultaneously solidified after sequential amplitude light patterns are displayed into a rotating photoresin vial. In Xolography<sup>11</sup> and Light-Sheet 3D printing<sup>12</sup>, two intersecting beams of different colors are required to perform the polymerization process, while dynamic light patterns are projected into the photosensitive resin.

Currently, most VAM techniques rely on amplitude patterns, commonly displayed using Digital Micromirror Devices (DMDs). These binary amplitude light modulators operate in reflection mode by tilting their micromirrors between two states: “on” and “off”. In the “on” state, a micromirror directs light to illuminate a corresponding pixel or voxel on the printing plane, while in the “off” state light is directed elsewhere. DMDs generate grayscale patterns by rapidly toggling micromirrors

Correspondence: Maria Isabel Álvarez-Castaño (maria.alvarezcastano@epfl.ch) or Christophe Moser (christophe.moser@epfl.ch)

<sup>1</sup>Laboratory of Applied Photonics Devices, School of Engineering, Ecole Polytechnique Fédérale de Lausanne, Lausanne CH-1015, Switzerland. <sup>2</sup>Present address: BIOINSIDE Lab, Department of Mechanical and Aerospace Engineering (DIMEAS), Politecnico di Torino, Turin 10129, Italy

© The Author(s) 2026



**Open Access** This article is licensed under a Creative Commons Attribution 4.0 International License, which permits use, sharing, adaptation, distribution and reproduction in any medium or format, as long as you give appropriate credit to the original author(s) and the source, provide a link to the Creative Commons licence, and indicate if changes were made. The images or other third party material in this article are included in the article's Creative Commons licence, unless indicated otherwise in a credit line to the material. If material is not included in the article's Creative Commons licence and your intended use is not permitted by statutory regulation or exceeds the permitted use, you will need to obtain permission directly from the copyright holder. To view a copy of this licence, visit <http://creativecommons.org/licenses/by/4.0/>.

between the ‘on’ and ‘off’ states, effectively controlling average light intensity. Recently, a holographic approach applied to tomographic VAM using phase encoding has been demonstrated<sup>13</sup>. Holographic projection enables capabilities beyond conventional amplitude-coded TVAM, including precise control of the point spread function (PSF), digital refocusing, aberration correction, and improved light efficiency. The system called HoloVAM<sup>13</sup>, used Lee Holograms to enable the use of the binary DMD modulator as a fast phase modulator<sup>14,15</sup>. However, such a phase modulator suffers from poor light efficiency (< 10%)<sup>13,14</sup>.

For decades, Liquid Crystal on Silicon (LCOS) Spatial Light Modulators (SLMs) were the only commercially available option for phase spatial light modulation. This device consists of electrically addressable pixels containing long chains of liquid crystal (LC) molecules positioned between two electrodes<sup>16,17</sup>. The alignment of LC molecules changes in response to an applied voltage, following the direction of the electric field. This realignment alters the intrinsic birefringence, resulting in phase and thus wavefront modulation<sup>16</sup>. Due to the LC molecule’s viscosity, the standard frame rate range of the LCOS SLM is between 60–120 Hz. LCOS SLMs typically degrade when operated under UV light<sup>18,19</sup>. Recently, Texas Instruments introduced a new type of MEMS-based Phase Light Modulator (PLM) that provides phase retardation thanks to the vertical displacements of the mirrors in a piston fashion. The vertical motion of each micro-mirror can be independently addressed with a 4-bit displacement resolution (16 states or mirror levels). Currently, the evaluation module (EVM) offers frame rates of up to 1440 Hz and a fill factor of 95%, providing high speed and light efficiency. Since the PLM does not rely on LC molecules, it is less subject to pixel crosstalk, is polarization-insensitive, and stable in phase as it has no molecular relaxations<sup>20</sup>. Due to these advantages, PLMs are gaining significant interest in applications such as wavefront shaping, holographic projection, and augmented reality displays<sup>21,22</sup>.

In this work, we demonstrate the first VAM system implemented using the new MEMS phase-only modulator (i.e. PLM). We first measure and calibrate the 16 phase levels (4-bit) of the PLM using an interferometric method which uses a self-generated diffraction phase grating<sup>23</sup> (see in Material and Methods section). We then measure the power efficiency of the holographic projections using the PLM and compare it with that of amplitude and phase encoding using a binary DMD. We experimentally found that pattern projections using the PLM is twice more efficient than using Lee holograms on the DMD for HoloVAM and 70-folds more efficient than amplitude. To leverage the PLM in the Holographic TVAM, we introduce a new hologram generation pipeline for computing

holographic projections with reduced speckles. For each projection angle, an axicon phase pattern is used to extend the depth of field in the reconstructed intensity pattern for a larger printing range along the direction of propagation after the Fourier lens. The pattern retention achieved with the axicon phase pattern is superior to a Gaussian beam profile over the diameter of the printing vial. To reduce speckles in holographic intensity reconstruction, the reconstruction is digitally shifted laterally in a time sequence using nine distinct axicon phases, each with its vertex shifted to a different position, such that the averaging process during the printing greatly smooth out the speckles. Excellent print surface quality is achieved with a carefully chosen lateral displacement. Then to demonstrate the light efficiency, and extended capabilities of the HoloVAM light engine using a phase-only light modulator (PLM), we printed multi-scale objects with acrylate-based resins and soft hydrogels. For the first time, we showcase the capability to print large-scale objects (up to 3 cm × 3 cm × 4 cm) as well as highly concentrated cell-laden hydrogels (1 million cells/mL) by employing gelatin metacryloyl (GelMA) and gelatin thiol/norbornene with the holographic TVAM technique.

## Results

The optical setup of our holographic TVAM (HoloVAM) system using a Texas Instruments (TI) DLP67750 PLM is shown in Fig. 1a. The light source is a 405 nm single mode laser diode. The PLM is positioned in front of a Fourier lens and a glass vial containing a photosensitive resin is placed at the conjugate plane (CP) of the focal plane of the lens L1 (See the Methods section for a detailed description of the setup). During the printing process, the vial is rotated continuously at a speed determined by the PLM frame rate, and a sequence of pre-calculated full-size holograms are projected to the resin. When High-Definition Multimedia Interface (HDMI) is used, the frame rate is 720 Hz and the vial rotation speed is 30 degrees per second. When Display Port (DP) is used, the frame rate is 1440 Hz and the rotation speed is 60 degrees per second. The PLM uses 16 discrete phase levels from 0 to  $2\pi$  using 4 bits of data. The phase modulation is imparted by the micromirrors’ vertical displacement as Fig. 1b illustrates. During holographic reconstruction, a linear phase ramp is added to the hologram on the PLM to separate the reconstructed intensity pattern from the zeroth order by directing the desired first diffraction order to pass through a spatial filter (SF) for printing, which blocks all other diffraction orders, including the zeroth order. Details of the PLM operation and calibration method can be found in the Methods section.

Figure 1c shows a comparison of the pattern light efficiency among two amplitude and phase-encoded

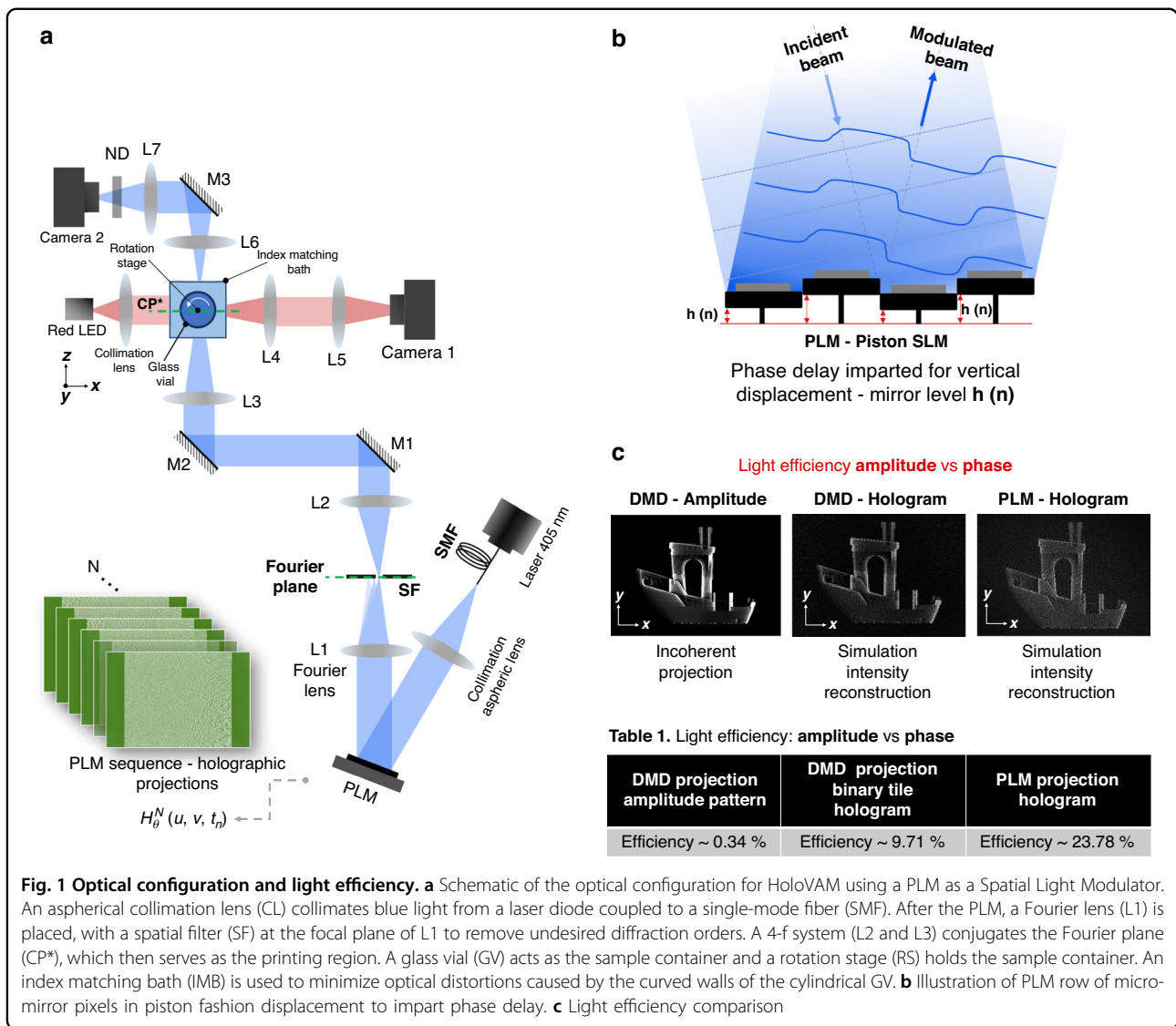


**Fig. 1 Optical configuration and light efficiency.** **a** Schematic of the optical configuration for HoloVAM using a PLM as a Spatial Light Modulator. An aspherical collimation lens (CL) collimates blue light from a laser diode coupled to a single-mode fiber (SMF). After the PLM, a Fourier lens (L1) is placed, with a spatial filter (SF) at the focal plane of L1 to remove undesired diffraction orders. A 4-f system (L2 and L3) conjugates the Fourier plane (CP\*), which then serves as the printing region. A glass vial (GV) acts as the sample container and a rotation stage (RS) holds the sample container. An index matching bath (IMB) is used to minimize optical distortions caused by the curved walls of the cylindrical GV. **b** Illustration of PLM row of micromirrors in piston fashion displacement to impart phase delay. **c** Light efficiency comparison

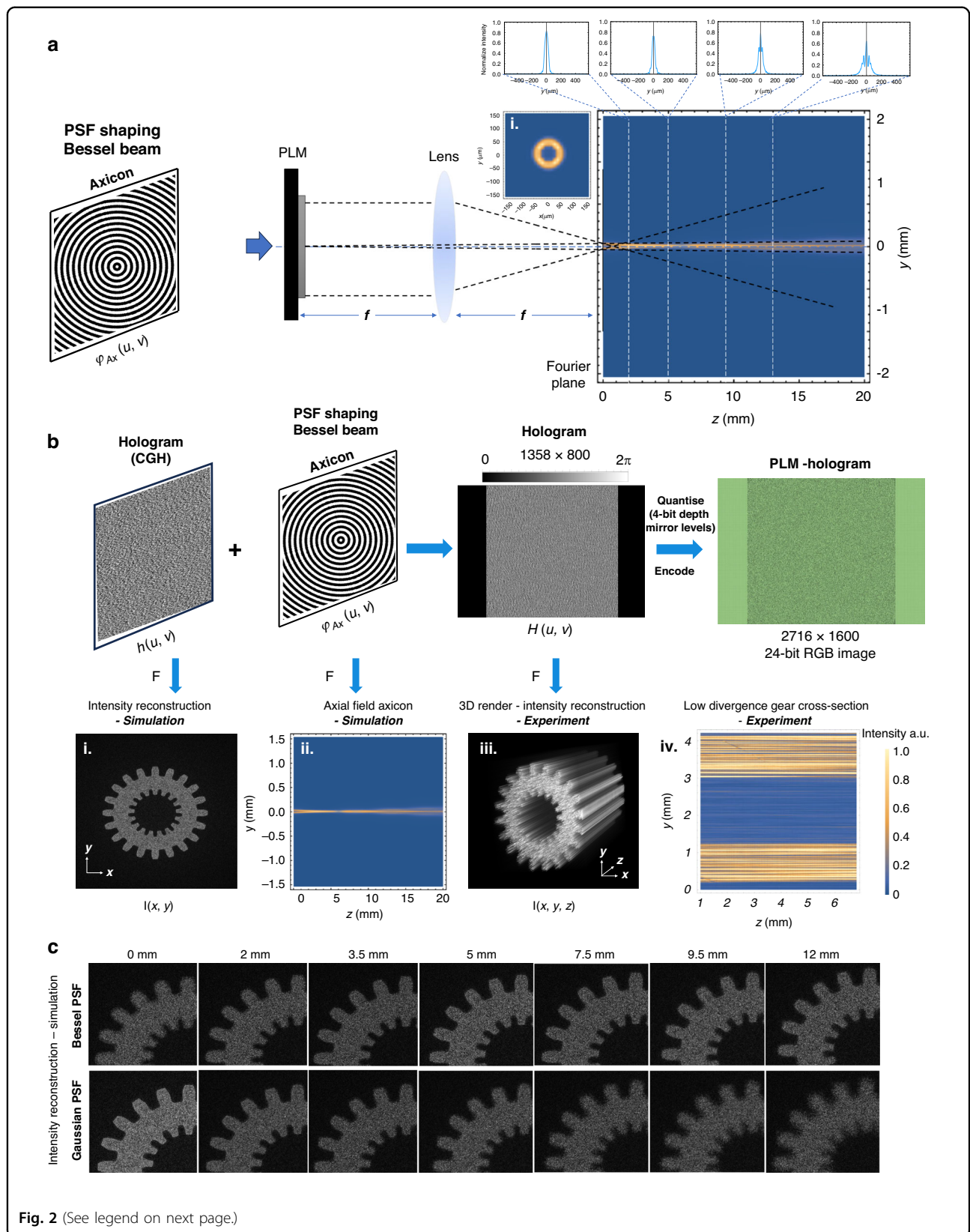
projections on a DMD (Table 1. left and center columns) and phase-encoded projections using a PLM (Table 1. Right column). We construct our setup (see details in Supplementary Information Fig. S1) in such a fashion that combines a DMD and a PLM so that experimental power efficiency can be compared.

A blazed grating using a multi-level phase-only modulator between 0 and  $2\pi$  has a theoretical diffraction efficiency close to 100% (98.7%) in the first order of diffraction for 16 levels. Experimentally, we achieved a diffraction efficiency for a blazed grating close to 45%. This efficiency loss is due to the fill factor of the PLM (95%), reflectivity of the mirrors at 405 nm, and a 20% light loss resulting from to the internal PLM operation, in which the micromirrors are reset to zero position for a period of 140  $\mu$ s every 694  $\mu$ s within a frame. This sequence is defined by the base PLM firmware installed in the EVM. The 140  $\mu$ s period

corresponds to the time when the hologram is loaded into the device. This does not affect the print because the zero order reflection from the PLM is blocked by the spatial filter in the Fourier plane (see Fig. 1). When a pattern is encoded, the absolute efficiency is close to 24%. With this latter efficiency value, the PLM light engine is approximately 70-fold more efficient than amplitude projections and twice more efficient than DMD holographic encoding previously reported for a holographic engine used in TVAM<sup>13</sup>.

**Holographic projections: computation pipeline**

The phase patterns were computed following the pipeline shown in Fig. 2 (for an extended description, see in Supplementary Note 2). Our technique is based on the tomographic method, where different approaches are used to calculate the amplitude patterns. The Radon transform assumes straight light rays (ray optics).



(see figure on previous page)

**Fig. 2 Hologram Computation for printing with PLM.** **a** Illustration of the working principle of the Bessel Beam generated with an axicon. i shows the ring intensity distribution in the focal plane (Fourier Plane), which is characteristic of axicons. Profiles of the axial intensity propagation of the axicon are shown on the top where the axicon region starts after 2.5mm in the near field region. **b** Pipeline for Computing the Holographic Projection  $H(u, v)$ . A CGH  $h(u, v)$  computed by GS Algorithm using an amplitude tomographic projection as the target intensity is convolved with an Axicon phase  $\varphi_{Ax}(u, v)$ . i Intensity reconstruction of a gear in the Fourier plane. ii Intensity profile of the axicon along with the propagation direction. iii–iv shows a 3D rendering and cross section of the smeared information when the phase of the gear is convolved with the axicon. **c** Simulation of the intensity reconstruction of a single holographic projection of an extruded gear. Top: Using a Bessel PSF. Bottom: Using an unmodified Gaussian PSF

However, this assumption fails at small feature size due to diffraction. A recent theoretical study shows that below approximately  $20\ \mu\text{m}$  feature size, the straight-ray assumption is no longer valid, and wave optics must be considered<sup>24</sup>. In order to achieve a uniform resolution across the print volume in practice, the depth-of-focus of the Gaussian diffraction limited beam is chosen to match the diameter of the vial. In our setup, for example, the resin container has an inner diameter of approximately  $11\text{mm}$ , which limits the printable feature to greater than  $54\ \mu\text{m}$ , assuming a Gaussian beam (See further explanation in Supplementary Note 3). To effectively extend this depth-of-focus to fulfill the collimation assumption of the Radon transform, we modify the Point Spread Function (PSF) of the system to form a Bessel beam using holographic projection. The Bessel beam PSF produces a pattern that shows an extended collimated projection length compared to a Gaussian PSF.

In our setup, the printing region is effectively located after the Fourier plane of the PLM. During the hologram pipeline construction process, we first generate an axicon phase  $\varphi_{Ax}(u, v)$ , which serves to generate low-divergence beams in the printing region, as shown in Fig. 2a. This axicon phase pattern is then added to the Computer Generated Hologram (CGH) phase pattern  $h(u, v)$  retrieved from the intensity pattern of tomographic projections of the voxelized 3D model<sup>1,10</sup> using the Gerchberg-Saxton (GS) algorithm. At the Fourier plane of the PLM, the reconstructed wave front is a convolution between the wave front of the CGH  $h(u, v)$  and that of the axicon phase  $\varphi_{Ax}(u, v)$ . After a short propagation distance beyond the Fourier plane, the reconstructed wavefront forms the desired projection image in which each bright pixel is a Bessel beam that stays focused over a distance much larger than the depth-of-focus of the same image without the axicon, as shown in Fig. 2b (i) - (iv). Once the holographic projection pipeline is created, the stack of phase maps is sent to the PLM control software, which down-samples the phase to 4-bit, encode it properly into video frames for PLM control, and play the frames on the PLM screen. See PLM operation in the Methods section for more detail.

### Speckle evaluation and reduction

Speckle refers to the high-contrast granular interference pattern commonly observed in optical reconstructions of

Computer-Generated Holograms (CGHs) displayed on Spatial Light Modulators (SLMs). Essentially, speckle is a result of the coherent superposition of a large number of wave fronts. In our system, the lack of amplitude modulation, the nature of imperfect phase retrieval from the GS algorithm, the pixelation of the PLM, defects in experimental conditions such as dusts and unwanted reflections all contribute to generate a speckle image in the printing region. Speckle in CGHs can be minimized using various techniques, including random phase methods, time multiplexing<sup>24</sup>, tiling holograms<sup>17,25,26</sup>. Recent approaches also explore the use of Neural Networks for time-multiplexed speckle reduction<sup>27</sup>.

Here, we use averaging of spatially shifted reconstructions to effectively reduce the speckle noise. This approach involves time multiplexing up to  $N_p = 9$  holograms per projection angle, each representing the holographic projection convolved with one of the 9 axicon phase laterally shifted off-vertex as illustrated in Fig. 3a, b (see details in the method section). The result is a series of projections shifted around the axicon vertex position that, when played sequentially, reduces the speckle noise through the averaging effect in the photopolymerization during printing, which greatly enhances the surface quality of the printed objects. The optimal offset is determined by analyzing the speckle grain size using the power spectrum density (PSD)<sup>28</sup> of the image of the intensity reconstruction of projected holographic pattern<sup>29</sup>, where the speckle grain size is  $43.42\ \mu\text{m}$  (See Supplementary Note 4).

Three different offset groups were used. A series of axicon phase patterns define each offset group shifted laterally from the central vertex in 9 different positions, as shown in Fig. 3a. When the resulting holograms are displayed sequentially (time-multiplexed), statistically some peaks of the speckles will coincide with some valleys, reducing the contrast of the speckle intensity compared with a single projection.

The level of speckle reduction is analyzed with the speckle contrast coefficient, a commonly used metric to quantify the speckle level of an image<sup>28–30</sup>.

$$c = \frac{\sigma_I}{\langle I \rangle} \tag{1}$$

where  $\sigma_I$  is the standard deviation of the image intensity and  $\langle I \rangle$  is the mean image intensity.

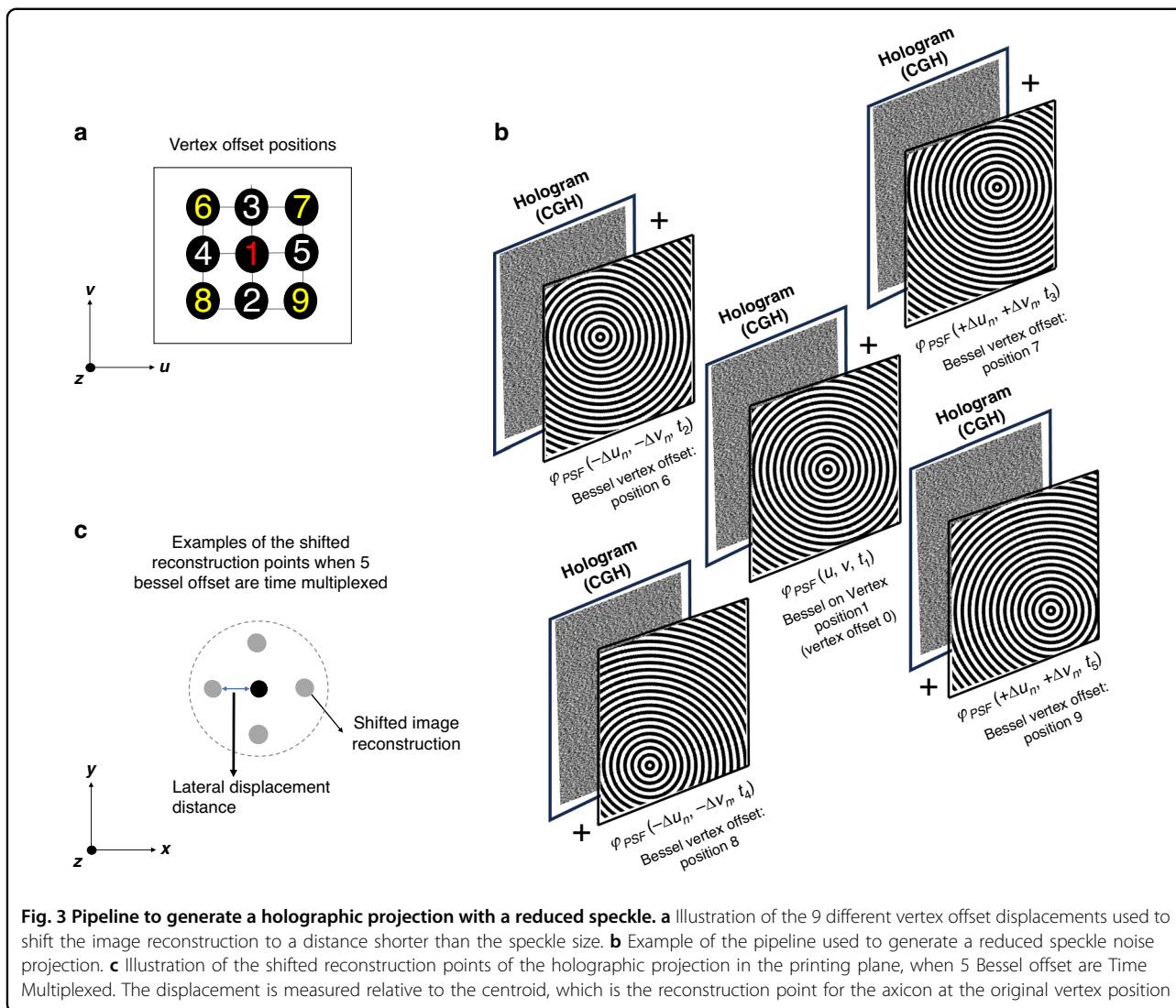
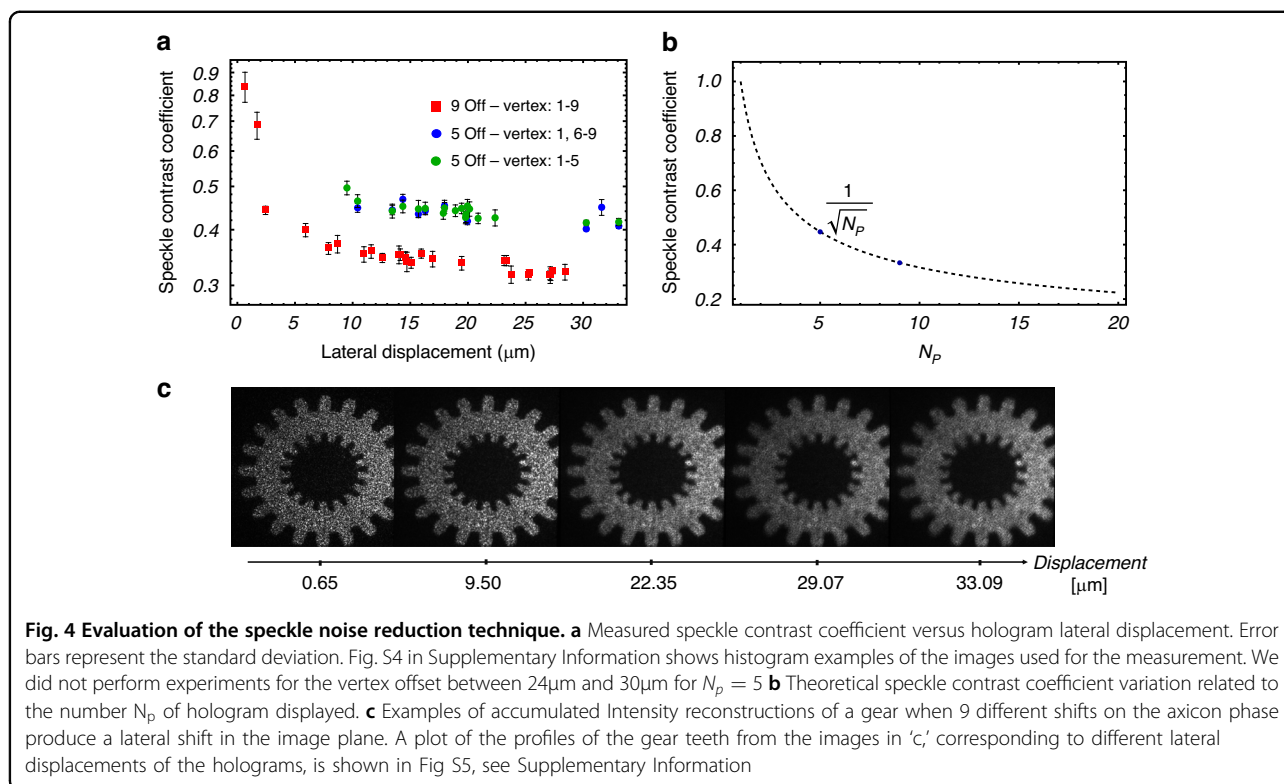


Figure 4a shows the speckle contrast coefficient as a function of the axicon displacement distance from  $1\ \mu\text{m}$  to  $33\ \mu\text{m}$  with different number of holographic projections  $N_p$ . The speckle contrast coefficient reaches a minimum when the lateral displacements are approximately half the speckle grain size, at which the likelihood of the speckle peaks in one image coincide with the valleys in another is maximized. This trend is statistically confirmed in Fig. 4b. Specifically, for  $N_p = 5$ , the minimum speckle contrast coefficient is  $c = 0.45$ , while for  $N_p = 9$ , the minimum possible value is  $c = 0.33$ . These results indicate that the optimal displacement distance, relative to the speckle grain size effectively reduces speckle contrast. From Fig. 4c, we can observe that the intensity reconstruction appears smoother, less grainy when the displacement is close to half the speckle grain size, expecting that, for printing, the surface quality of the printed objects should improve.

### Multi-scale printing with speckle-reduced holographic projections

To demonstrate the capabilities of our PLM-based light engine for volumetric printing, we successfully fabricate multi-scale objects using holographic projections and the speckle reduction approach described above. Three different photosensitive resins were used in the prints: one acrylate and two hydrogels. First, we used a commercial polyacrylate resin with Diphenyl (2,4,6-trimethylbenzoyl) phosphine oxide (TPO) as the photoinitiator (PI) at a concentration of 1 mM. Thanks to the efficient light engine, we fabricated objects at multiple scales through digital scaling of the holographic projection, as shown in Fig. 5. Figure 5a shows a  $4\text{mm}$  high fusilli 3D model printed in 32 seconds using a laser output power of 18 mW. Figure 5b shows a large and small Stanford Bunny model. The large model is  $8\text{mm}$  high and printed in 61 s with 50 mW laser output power, while the small model is

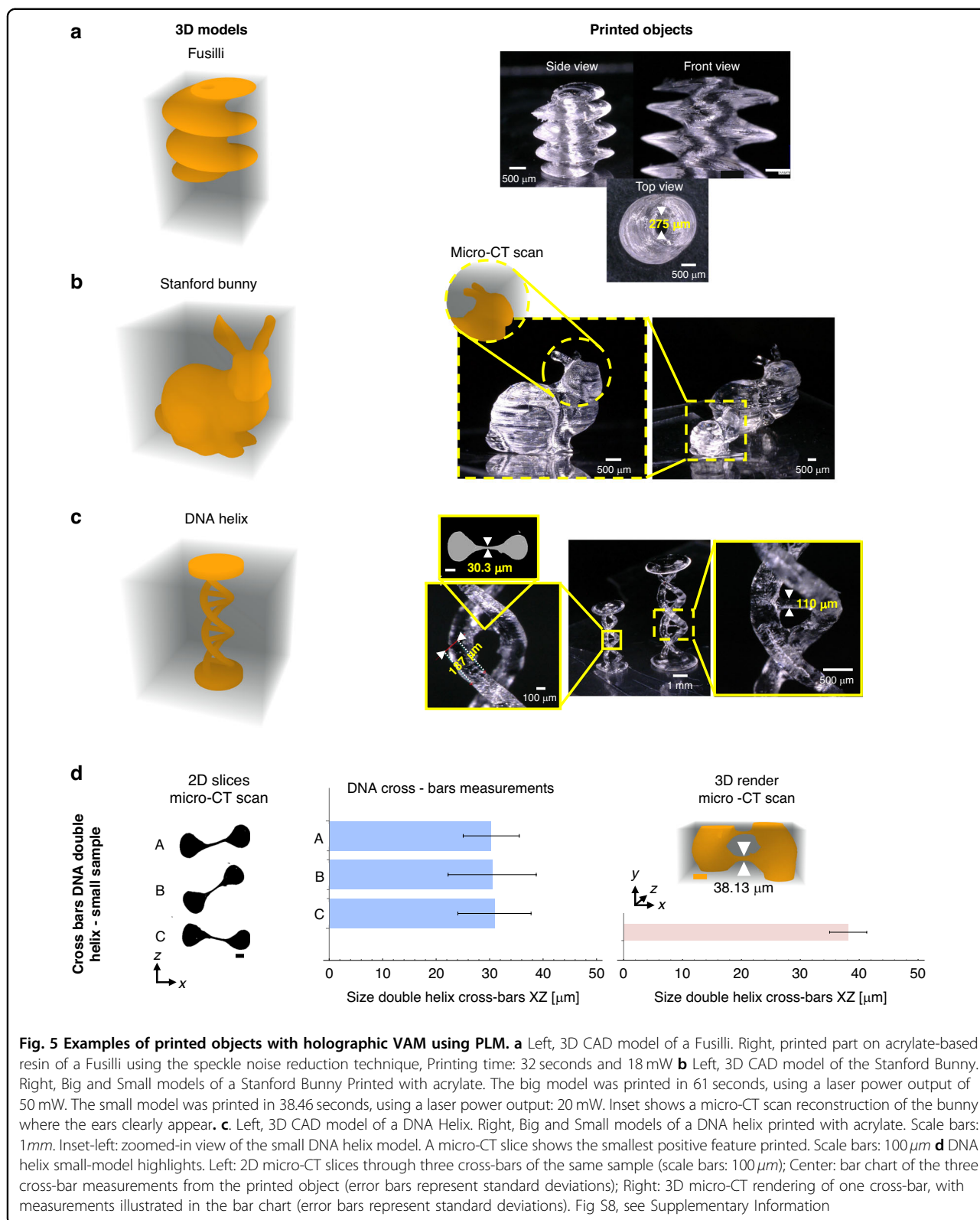


4mm high and printed in 38.5 s using 20 mW laser output power. Figure 5c shows a large and small model of a DNA double helix. The small model was printed in 23 s using 20 mW laser output power. The zoomed inset of the large and the small models shows the good surface quality achieved with the speckle reduction technique. Figure 5d shows highlights from the small-size DNA helix model, including the smallest positive feature printed, a DNA helix cross-bars measuring  $\sim 30.3\ \mu\text{m}$  (XZ) and  $\sim 38.13\ \mu\text{m}$  laterally (XY). The targeted lateral feature was  $\sim 39.9\ \mu\text{m}$ . In contrast, the lateral (XY) dimension of the larger sample measured  $\sim 47.15\ \mu\text{m}$ , versus the expected  $\sim 53.2\ \mu\text{m}$ . Fig. S8 in Supplementary Information illustrates these measurements with standard deviations, expected values, and model dimensions. The size difference arises from oxygen diffusion, which typically limits sub-100  $\mu\text{m}$  features in photocurable resins. Only three cross-bars remain in the illustrated model, the others broke during post-processing due to their small size, fragility, and oxygen diffusion effects. We also calculated Jaccard indices between micro-CT scans and the model. Values of 0.83 for the large model, and 0.66 for the small model were encountered (see Supplementary Note 8, Fig S8.1). This difference reflects oxygen diffusion's stronger impact on small-scale samples.

Figure 6 shows a DNA double helix printed using holograms without and with the speckle noise reduction technique. Figure 6a shows a photo of the printed object

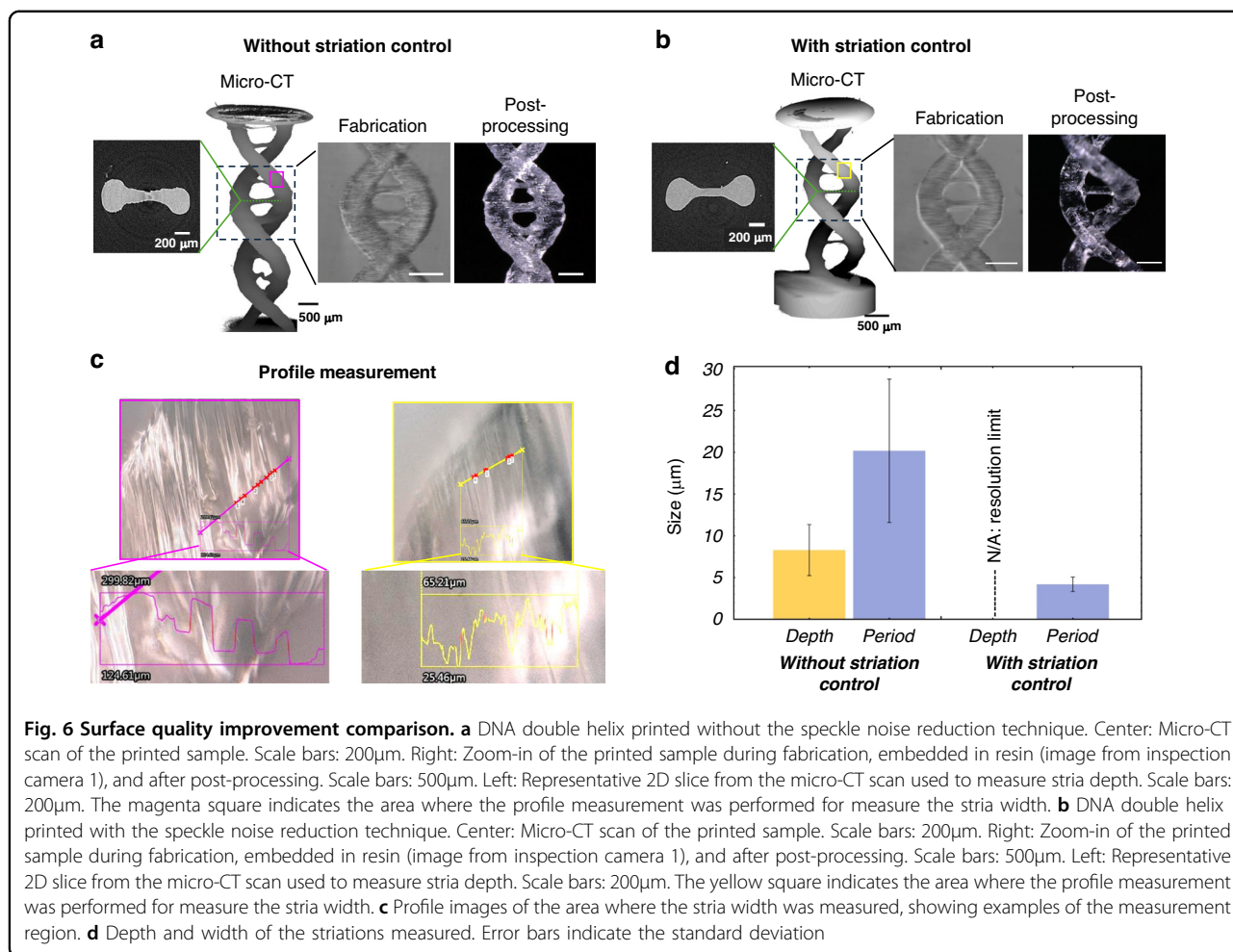
without the speckle noise reduction technique. Figure 6b shows a photo of the printed object printed with the speckle noise reduction. The granular pattern of the speckle introduces intensity gaps between the bright grains, which are visible in images captured by inspection camera 1. The application of the speckle noise reduction technique results in visibly smoother surfaces. With reduced granularity in the holograms, there are fewer intensity gaps between the bright grains of the speckles, which in turn diminishes the formation of filaments, due to the self-focusing effect during the polymerization process, that can later cause delamination in the printed objects. We also calculated the Jaccard index for the samples shown in Fig. 6. Values of 0.83 and 0.80 were found for samples with and without stria control, respectively. These results show that stria control not only improves surface quality but also enhances the overall fidelity of the sample (see Supplementary Note 8 and Fig. S8.1).

A gelatin methacryloyl (GelMA) hydrogel laden with human fibroblasts (HFF-1) was used to demonstrate the printing capability of holographic VAM using a phase light modulator (PLM) in scattering resins for biofabrication. A 3D model corresponding to a multiacinar construct (Fig. 7a), designed to mimic the tubuloacinar structures of the exocrine pancreas<sup>31</sup> was printed<sup>13</sup>. Unlike previous reports using the holographic VAM method<sup>13</sup>, the samples in this study were printed with



Bessel beams in a hydrogel containing twice the cell concentration ( $1 \times 10^6$  cells  $\text{mL}^{-1}$ ; see Materials and Methods). In addition, the printed constructs had an

approximately 8-fold larger volume, resulting in structures that were about twice as large in each dimension ( $\sim 4 \text{ mm} \times 4 \text{ mm} \times 4 \text{ mm}$ ) compared with those

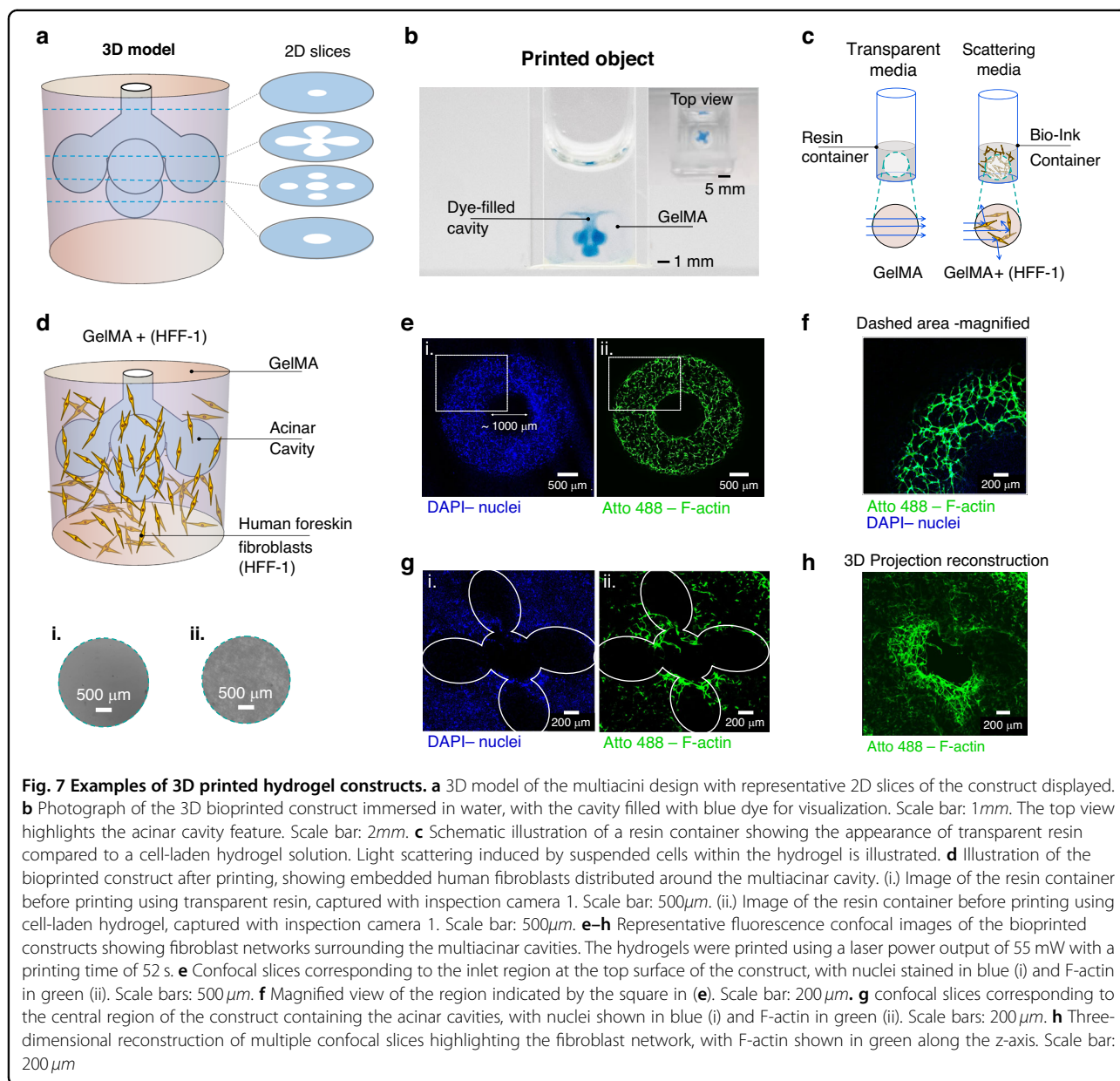


previously achieved. The printed hydrogel constructs closely matched the target geometry (Fig. 7a, b). Filling the internal cavities with blue dye enabled direct visualization of the acinar features and verified the continuity and accessibility of the internal lumen (Fig. 7b). To illustrate the challenging optical environment during printing, we compared the appearance of the resin container filled with transparent resin (non-scattering media) and with a cell-laden hydrogel solution (scattering media), Fig. 7c. Real images from inspection camera 1 shows transparent resin appeared optically homogeneous (Fig 7d-i), the presence of cells within the hydrogel introduced visible light scattering (Fig 7d-ii).

Following printing, fluorescence confocal microscopy was used to visualize cell organization and cytoskeletal structure within the printed constructs (Fig. 7e-h). Fibroblasts exhibited an elongated morphology throughout the full depth of the constructs.

To illustrate the potential enabled by the improved light efficiency of the light engine, we built an additional setup to print large-scale models. This time, the system

magnification is 9 X, allowing us to print structures up to 3 cm×3 cm x 4 cm (the schematic of the experimental setup is shown in Fig S6, Supplementary Note 6). The setup uses the same PLM and light source. Figure 8 illustrates an example of a large-scale sample printed with gelatin Thiol/Norbornene (Gel-SH/NB), and Lithium phenyl-2,4,6-trimethylbenzoylphosphinate (LAP) as photoinitiator (see Materials and Methods). The sample was printed using the speckle noise reduction technique described previously to achieve better surface quality and prevent delamination. The printing time for this large-scale Human Ear sample was 2 min and 12 s, using an output laser power of 150 mW at 405 nm. Gel-SH/NB is known to be much more reactive than GelMA at the same concentration of photoinitiator, offering better structural definition and enhanced resolution thanks to its lower sensitivity to oxygen diffusion compared to conventional (meth)acrylate-based resins. The light engine's efficiency is clearly demonstrated, since to print objects of size 1 cm<sup>3</sup>, conventional TVAM methods use light sources with power around 6 W<sup>1,10</sup>. Moreover, similar scale

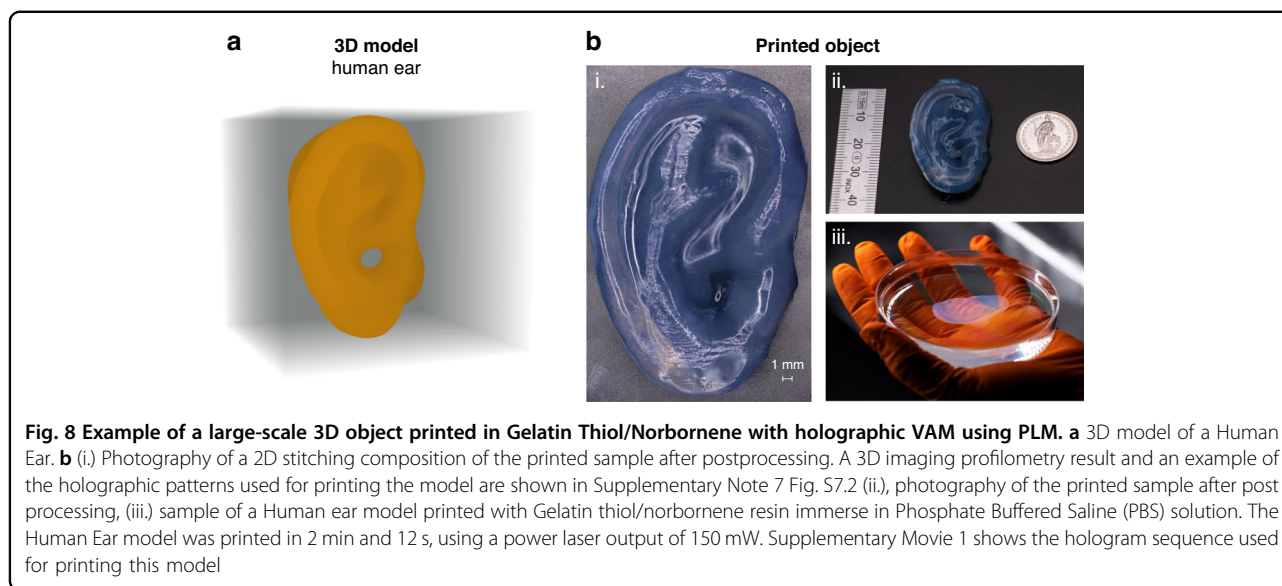


samples were printed before using the Helical TVAM<sup>32</sup> method, for which the used light-source was 1.8 W, and the printing time using acrylate-based resin was up to 10 minutes. For comparison, the same Human Ear model was printed with commercial acrylate resin on the same scale (3 cm  $\times$  3 cm  $\times$  4 cm), which took 7 min and 45 seconds (see Supplementary Information Fig. S7.2), where thanks to the speckle noise reduction technique the surface quality is smoother showing transparency. We also printed the same model at a different scale (1.5 cm  $\times$  1.5 cm  $\times$  2.5 cm) by scaling down the target intensity for the calculated holographic projections, completing the print within 5 min (see the printed sample in Supplementary Note 7 Fig. S7.1).

## Discussion

In this work, we have demonstrated the potential of using the new MEMS-based, fast, phase-only modulator (PLM) in Holographic TVAM, which is capable of modulating light at a frame rate up to 1440 fps for holographic printing, marking a significant leap in holographic projection technology. By integrating the PLM, we achieved 70-times more efficient light engine for HoloVAM, enabling faster print times, high-fidelity printed parts and scale from 1 mm<sup>3</sup> to 36 cm<sup>3</sup> in a few minutes.

We presented the software control scheme for the DLP6750 PLM EVM. It is implemented in an in-house MATLAB program that quantizes the phase sequence to 4 bits, encodes it into display frames for PLM control, and



plays the frames at a constant rate without loss. We also developed a characterization method to measure and calibrate the PLM phase response. Accurate mapping of phase retardance to the corresponding 4-bit voltage bias improves the efficiency of holographic reconstruction. We also introduced a computational pipeline to calculate the holographic projections. We also mitigated the effect of the speckle by using a time-division multiplexing method where a series of grouped CGHs per angle convolved with up to 9 different PSF off vertex allows us to improve the light dose while reducing the speckle noise.

Our work shows that using a PLM in holographic 3D printing enables fast fabrication of multi scale objects using low-power, cost-effective light sources. Furthermore, we demonstrate this approach with diverse materials, including acrylate-based resins, soft hydrogels, and cell-laden hydrogels.

Our speckle-reduction method achieves prints with smooth surface quality, comparable to blurred tomographic printing<sup>33</sup> implemented with LED light sources. LED-based VAM typically relies on diverging illumination (and associated optical aberrations) to suppress striation artifacts, making them particularly well suited for the fabrication of smooth, continuous geometries such as lenses. However, the achievable construct size is constrained by both pattern efficiency and the limited optical power available from LEDs. The diverging beams also impacts the attainable spatial resolution. In this work, we observed that time-multiplexing axicons to laterally shift the projection patterns leads to a pronounced surface smoothing effect compared to conventional laser-based amplitude TVAM. This approach was initially introduced as an alternative strategy for speckle-noise reduction and was subsequently found to also reduce striation artifacts.

This behavior is distinct from previously reported HoloVAM implementations, in which the speckle-noise reduction strategy (HoloTile) resulted in the generation of pronounced striations.

In addition, we experimentally observed that using our holographic light engine together with a Bessel point spread function (PSF), enables printing in scattering media without the need to pre-compensate light patterns, as required in conventional TVAM, where characterization of each individual sample is necessary. We believe that the self-healing properties of the Bessel beam may contribute to this effect. Our method offers a clear advantage, eliminating the need for correction or characterization of each sample as required in conventional TVAM.

Experiments involving cells embedded in hydrogel formulations further confirm the feasibility of this approach for biofabrication applications. Notably, we successfully printed cellularized constructs substantially larger than those previously achieved using earlier HoloVAM strategies<sup>13</sup>, despite the increased light scattering associated with higher cell densities. This demonstrates the advantage of phase-only modulation for holographic printing in optically heterogeneous and scattering media, where conventional holographic approaches may suffer from reduced reconstruction fidelity.

Confocal fluorescence imaging performed six days after printing revealed well-defined fibroblast networks surrounding the multiacinar cavities. These observations confirm that neither the printing process nor the speckle-reduction strategy adversely affected cell viability. Moreover, the close agreement between the confocal images and the representative virtual slices shown in Fig. 7 indicates that the printed geometry is largely preserved

over time, even though cellular remodeling may induce minor shape changes.

We investigated the performance and advantages of a hologram-based light engine for tomographic volumetric additive manufacturing (TVAM) using a phase light modulator (PLM). The system enables the fabrication of multi-scale objects through digital scaling and enhanced light efficiency. Using a laser diode with a power output of up to 150 mW allowed us to print large-scale samples. ( $3 \times 3 \times 4 \text{ cm}^3$ ). Recently, Zhan et al.<sup>34</sup> demonstrated the printing of multiscale, large-volume structures via the incorporation of an amine additive in the resin which reacts with oxygen-derived peroxy radicals to regenerate active propagating radicals. We have demonstrated that incorporating materials following the same photochemistry as Zhan et al., such as Gel-norbornene, enables printing of large samples.

Nevertheless, we believe that improving projection fidelity in the Holographic TVAM technique remains essential. In this work, we enhanced pattern fidelity and light efficiency in the holographic VAM light engine by integrating a 4-bit (16 levels) phase SLM instead of the 2-bit modulator (DMD) used previously. However, the PLM still introduces phase quantization errors and pixel dependent voltage to phase that affect diffraction efficiency and pattern fidelity. These limitations highlight opportunities for future refinements, such as incorporating machine learning-based methods and camera in the loop approaches<sup>35</sup>.

To summarize, we believe that print quality limitations arise from both optical pattern projection fidelity and chemical inhibition. To obtain a more accurate 3D print fidelity, future work requires both to improve the holographic projection and importantly including a model that includes inhibition kinetics. The DNA helix cross-bars and bunny ears (Fig. 5) exemplify that oxygen quenching plays an important role in small structures.

We believe that incorporating oxygen diffusion in the holographic projection patterns optimization will further improve print fidelity for features  $< 50 \mu\text{m}$ . Other complementary solutions include the use of oxygen scavengers, resin additives, and gel-norbornene-like chemistries. Combined optical–chemical strategies will enhance quality while preserving the advantages of phase encoding.

## Materials and methods

### Experimental setup for 3D printing

The schematic of the optical setup for holographic tomographic additive manufacturing (HoloVAM) using a PLM as a spatial light modulator is shown in Fig. 1a. A fiber-coupled continuous wave (CW) 405 nm blue laser diode (Integrated Optics, 0405L-13A-NI-AT-NF) is used as the light source. This beam is collimated using an aspherical lens (CL) and then obliquely incident upon the PLM arranged in a Fourier configuration with the Fourier

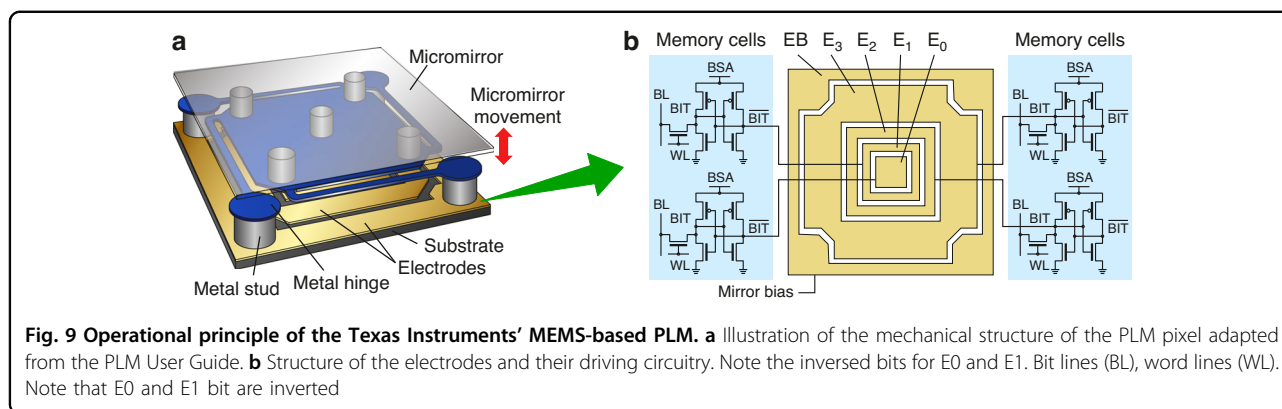
lens L1 (focal length  $f_1 = 180 \text{ mm}$ ), and a spatial filter (SF) is used to filter out the zero-order diffraction at the Fourier plane of L1. Lenses L2 ( $f_2 = 150 \text{ mm}$ ) and L3 ( $f_3 = 200 \text{ mm}$ ) form a 4-f system that conjugates the Fourier plane and rescales the holograms by 1.33 X in the printing plane (CP\*, Conjugate Fourier Plane). An index matching bath (IMB) is used to reduce the optical distortion caused by the curved interface of the glass vial. For large-scale objects the 4-f system is rescales by 9 X, using L2\* ( $f_2^* = 40 \text{ mm}$ ) and L3\* ( $f_3^* = 360 \text{ mm}$ ), see Supplementary Note 6.

A rotary stage (RS, Zaber- RSW60C-E03T7-KX13A) holds the sample vial (GV, glass vial), which is set to rotate at a constant speed of  $30^\circ/\text{s}$  when the PLM is using HDMI or  $60^\circ/\text{s}$  when DP is used. Because of the two different PLM frame rate possible settings, a different time per turn was set when the PLM interface was changed; when using the HDMI interface, the time per rotation is 12 seconds, and when using DP interface, the time per rotation is 6 seconds. Using the in-house MATLAB software, the PLM displays a sequence of holographic projections every  $\Delta\theta = 0.5^\circ$  at a frame rate of 720 Hz (HDMI) or 1440 Hz (DP), corresponding to light dose time per angle of  $\sim 16 \text{ ms}$  and  $\sim 8 \text{ ms}$ , respectively. The Trigger 2 output of the PLM is used as a counter to ensure precise synchronization between the rotation platform and the hologram sequence. A computer laser control program and a mechanical shutter are used to allow the laser to irradiate the resin sample at a specified power and for a given period. An index-matching bath of vegetable oil ( $n = 1.48$ ) is used to mitigate the lensing effect caused by the cylindrical vials containing the photoresin when the acrylate-based are use, and water ( $n = 1.33$ ) when hydrogels are used.

Two inspection systems were incorporated to monitor the polymerization process and the holographic projections. The first system use a Red LED (R-LED) collimated using a collimation lens (CL) (polymerization monitor) employs lenses L4 ( $f_4 = 100 \text{ mm}$ ) and L5 ( $f_5 = 180 \text{ mm}$ ) with camera 1 (C1, iDS UI307xCP-M), while the second system (projections monitor) uses lenses L6 ( $f_6 = 75 \text{ mm}$ ) and L7 ( $f_7 = 100 \text{ mm}$ ) with camera 2 (C2, iDS UI327xCP).

### PLM operation

The Texas Instruments PLM is a phase-only SLM based on vertically moving micromirrors. The DLP6750 PLM EVM used in this work features a  $1348 \times 800$  pixel array with a pixel pitch of  $10.8 \mu\text{m}$  and uses a video interface (HDMI or DP) for data communication with the host computer. Figure 9 shows the operational principle of the PLM micromirror. The mechanical structure of the PLM pixel is shown in Fig. 9a. The micromirror (grey) sits on the metal hinge (blue), which is maintained at the voltage of the bias voltage electrode (EB) on the substrate. Four



control electrodes (E0 – E3) can be switched on or off to a control voltage. The potential difference between the control and the bias electrodes provides an electrostatic attraction force that is programmable depending on the number of control electrodes that are switched to the on state, causing the movement of the micromirror (red arrow). Consequently, the position of the micromirror modulates the phase of the reflected light. Figure 9b shows the structure of the electrodes and their driving circuitry. The micromirror actuation is controlled by four memory cells that are each connected to one of the control electrodes, the content of which is distributed from a computer through either a display interface or a universal serial bus. Owing to the memory cells, the PLM possess an important advantage of no flickering over liquid-crystal based SLMs. Furthermore, the PLM device is polarization insensitive, and adapting it to work with different wavelengths can be simply achieved through adjusting the bias voltage without the need for recalibration.

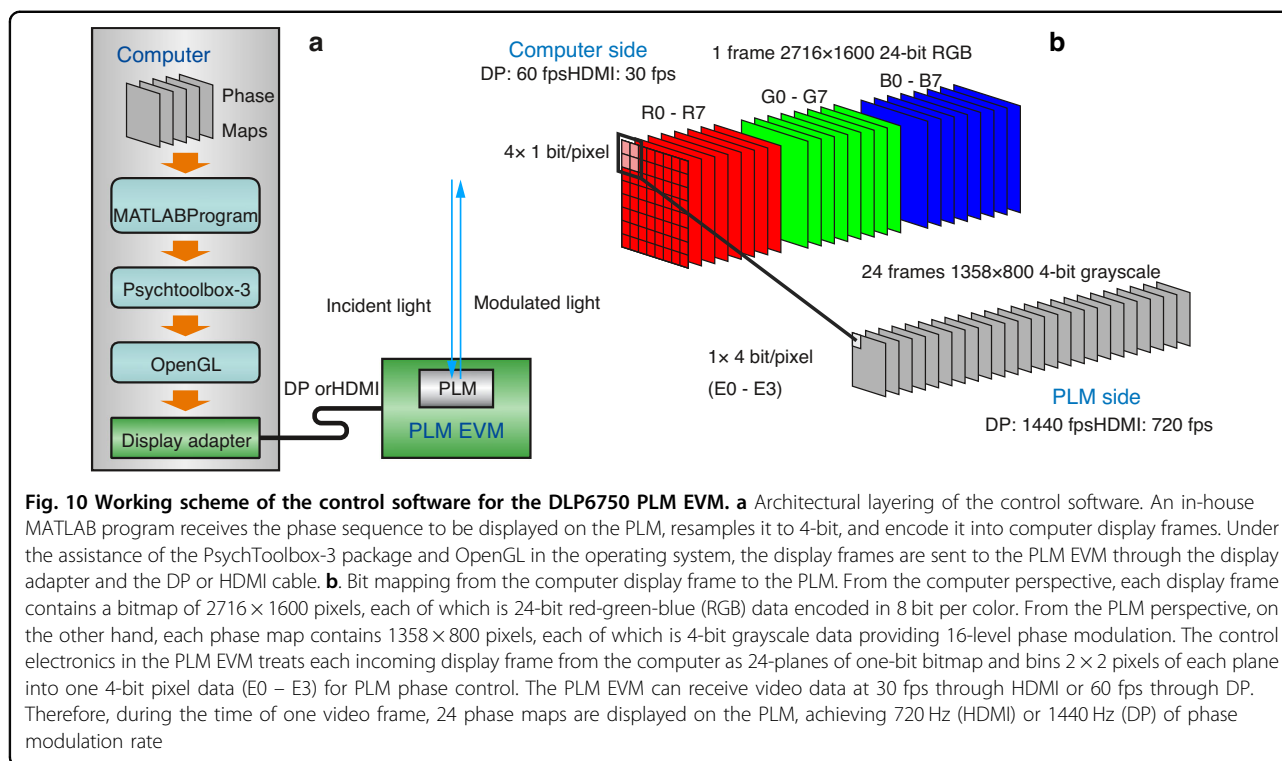
Figure 10 shows the working scheme of the control software for the DLP6750 PLM EVM. The architectural layering of the control software is shown in Fig. 10a. Once connected to a host computer through HDMI or DP, the PLM functions as an additional display screen of  $2716 \times 1600$  pixels on the computer side after basic configurations using a USB-based control software. The bit mapping from the computer display frame to the PLM EVM is illustrated in Fig. 8b. The actuation of each PLM pixel is controlled by four pixel bits from a  $2 \times 2$  pixel block in the corresponding 24-bit RGB display frame received from the computer video interface. This allows the PLM to interpret each received display frame data at  $2716 \times 1600$  pixel resolution as 24 frames of 4-bit micromirror positions at  $1358 \times 800$  pixels per frame, achieving a PLM frame rate of  $30 \times 24 = 720$  Hz and  $60 \times 24 = 1440$  Hz with HDMI (30 fps) and DP (60 fps) interface, respectively. The task of the control program is to reverse-encoding from the phase map required to be displayed on the PLM to the computer side so that each

phase map sequence can be correctly displayed on the PLM without frame loss. While the GPU-accelerated encoding step is completed offline, playing the encoded frames on the display adapter at the video rate must be performed in real time. While there is no guarantee for response time in a high-level programming language like MATLAB or Python and a time-sharing operation system such as Windows, we achieved nearly loss-free playing of phase maps owing to the support from Psychtoolbox-3 and the double-buffering capability of OpenGL without resorting to C/C++ program and DirectX.

### PLM calibration

The PLM is capable of producing a phase shift of up to  $2\pi$  for a wavelength range of  $405\text{nm} < \lambda < 650\text{nm}$ , which is wavelength-dependent. The PLM provides a mirror bias voltage control that is used to adjust the mirror displacement according to the wavelength. The calibration is achieved by measuring this phase delay as a function of the micro-mirror state.

A calibration was performed for the correct operation of PLM. Several phase calibration methods for phase-only modulators based on LCOS SLM have been reported in the literature. Common methods include phase shift interferometry based on the analysis of interference fringes obtained in a Michelson interferometer<sup>16</sup>, two-beam interferometry<sup>16,21</sup>, binary diffraction grating, and many others based on the Muller matrix and Jones vectors<sup>36–38</sup>. In contrast to LCOS, where the phase delay is based on birefringence and each pixel is a Pockels cell, the operation of the PLM is based on the phase delay imparted for vertical displacements of the micromirror. Therefore, the phase delay in each pixel is a function of the 4-bit response of the mirror position. Our calibration is an adaptation of an interferometric method that uses a self-generated diffraction grating<sup>23</sup>. Figure 11a shows the optical setup used for phase calibration. For this method, the image displayed on the PLM consists of two sectors, as shown in Fig. 11b. One part of the image consists of a binary grating, which is kept constant, while the other part



of the image is a uniform gray level that varies. These gray levels correspond to different mirror positions. When a collimated beam is incident on the PLM, the binary grating region diffracts the light, splitting the beam into several diffraction orders, while the uniform gray level region (piston) modifies the optical path of the reflected light. Consequently, the shifts in the resulting interference fringes between the diffracted and the reflected beams is proportional to the induced phase change in the reflected beam, which is used in our calibration.

**Time multiplexing of computer-generated holograms with lateral shift**

The lateral shift imparted to the holographic projections is achieved by convolving the CGH phase with axicon phases with different offsets. When these holographic projections are displayed sequentially over time, the accumulated intensity generates a holographic projection with reduced speckle noise, resulting in a smoother image as explained above. However, a small lateral shift produced by an axicon with its vertex off-axis can generate a slight angular divergence in the light intensity distribution during near-field propagation, which is also transferred to the intensity reconstruction of the desired shape when the holographic projection is convolved with an axicon off-axis (See Supplementary Information Note 2. Fig S2.1.a, b, angular shift of the axicon axil intensity).

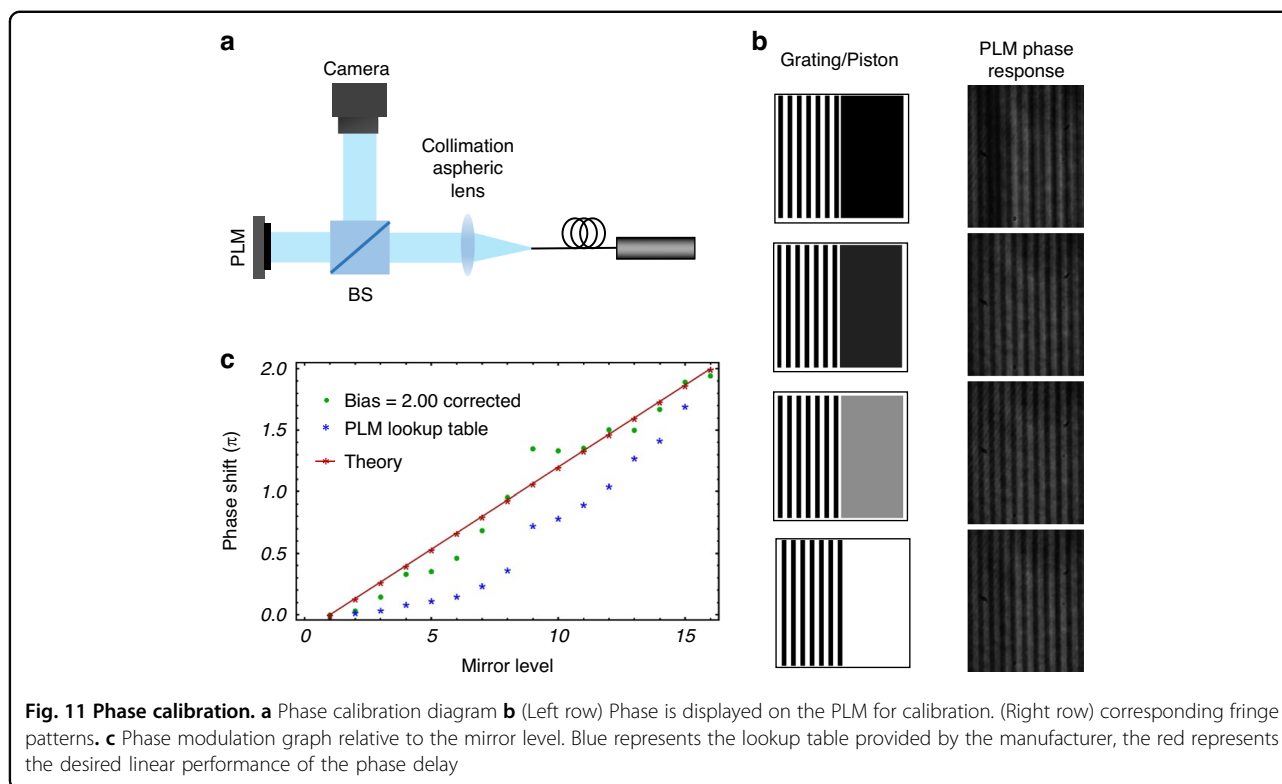
To evaluate the shift imparted to the holographic projection, we determined the intensity centroid position of

the reconstructed gear pattern along the propagation distance. The Intensity Centroid is a spatial intensity measurement that provides the coordinates of the intensity-weighted centroid, which we then track over the propagation distance. Figure 12a illustrates two examples of the shifts imparted to reduce speckle noise. The vertex shift generates a lateral displacement of the holographic projection in the y-direction of approximately  $\sim 12 \mu\text{m}$  (Fig.12a -top) and  $\sim 31 \mu\text{m}$  (Fig.12a -bottom). In both cases, a slight angular divergence of  $\pm 3 \mu\text{m}$  is noticeable along the propagation. However, when the time multiplexing of the holographic projections is performed, the centroid exhibits an average position that propagates parallel to the axicon on-axis, with a divergence of less than  $3 \mu\text{m}$ . The small fluctuations in the intensity centroid are due to changes in the speckle pattern during propagation, which are influenced by the Bessel intensity distribution of the point spread function (PSF). This effect enables us to achieve prints with smooth surface quality, similar to previous works such as blurred tomographic printing<sup>33</sup>.

**Photocurable resin**

**Acrylate**

Photoresin was formulated by combining the photoinitiator TPO (Diphenyl (2,4,6-trimethylbenzoyl)-phosphine oxide, Sigma) with commercial polyacrylate photoresin (PRO 21905, Sartomer) at a concentration of 1 mM. The resin has a viscosity of 20P s, at temperature.



The mixture of the resin with TPO was homogenized using a planetary mixer deaerator (Kurabo Mazerustar KK-250SE). The photocurable resin was subsequently transferred into cylindrical glass vials (12 mm outer diameter) and subjected to sonication to eliminate air bubbles. For large-scale samples, mixture preparation and formulation were kept similar; however, the resin container had an inner diameter of 30 mm. After transferring the resin to the glass vial, we introduced it to the vacuum chamber until the air bubbles were reduced. Later, the resin container was kept open in the fume hood overnight to avoid inhomogeneities in the sample polymerization.

### Hydrogels

**Gelatin metacryloyl (GelMA):** GelMA was synthesized from type A porcine gelatin (Sigma, G2500) following the protocol of Van De Bulcke et al.<sup>39</sup>. Briefly, the gelatin (10% w/v in Phosphate Buffered Saline (PBS), 50°C) was functionalized with methacrylic anhydride at 50°C for 3 h, then lyophilized and stored at -20°C<sup>31</sup>. For hydrogel preparation, lyophilized GelMA was dissolved at 7% w/v in PBS, and lithium phenyl-2,4,6-trimethylbenzoylphosphinate (LAP, Sigma-Aldrich, 900889) was added at 0.5 mg/mL as the photoinitiator. Before use, the photoresin was filtered through 0.2 μm filters both to ensure sterility for subsequent cell-based applications and to remove scattering particles that could interfere with the photopolymerization process.

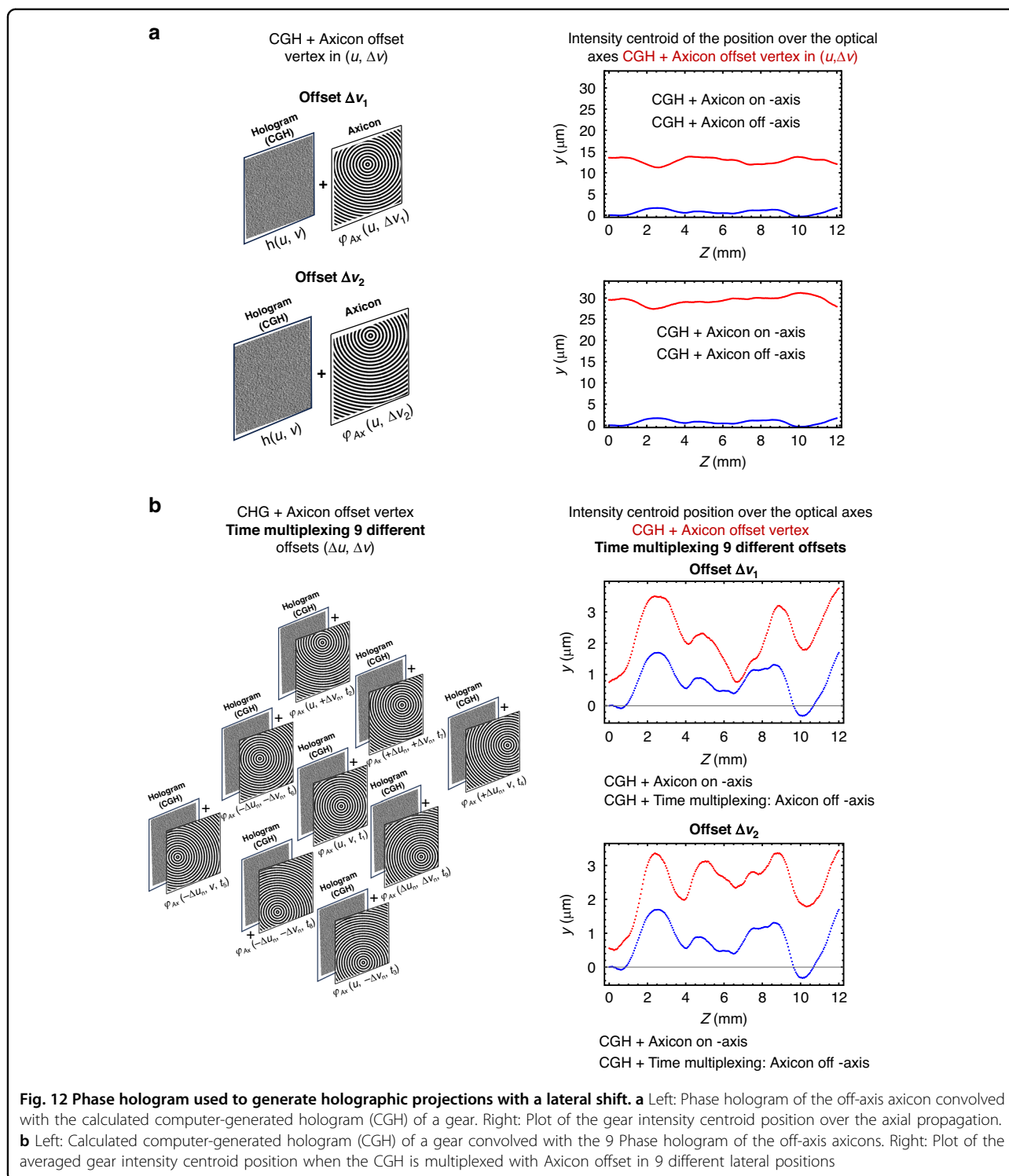
**Cell culture of HFF-1:** Human foreskin fibroblasts (HFF-1) obtained from ATCC® were cultured in DMEM without phenol red, supplemented with 1% penicillin streptomycin ptomycin, 2 mM L-glutamine, and 15% fetal bovine serum (all Gibco), and maintained at 37°C in 5% CO<sub>2</sub>.

**Gelatin thiol/norbornene resin (Gel-SH / NB):** The synthesis of gelatin-norbornene (Gel-NB) was performed as previously reported, and the degree of substitution was found to be ≈ 0.17 mmol/g<sup>40</sup>. The synthesis of gelatin-thiol (Gel-SH) was performed as previously reported<sup>40</sup>, and the degree of substitution was found to be ≈ 0.28 mmol/g. Freeze-dried Gel-SH and Gel-NB were dissolved at 5% w/v (total polymer concentration) in PBS at 37°C with 1:1 molar ratio of SH:NB. Photoinitiator lithium phenyl-2,4,6-trimethylbenzoylphosphinate (LAP) was added from a stock solution of 2.5% w/v in PBS to obtain a final concentration of 0.05% w/v. Before use, the photoresin was filtered (0.2 μm filters) to remove debris and scattering particles. The warm resin was poured into cylindrical glass vials (30 mm outer diameter) and left to thermally gel at 4°C for 15 min.

### Post-processing

#### Acrylate

Once printing was complete, the printed parts were extracted from the glass cylinders and immersed in propylene glycol monomethyl ether acetate (PMGEA) for a



10-minute rinse under gentle stirring using a vortex mixer. Subsequently, they underwent an additional 10-minute cleaning process in isopropyl alcohol (IPA). The printed samples were post-cured under UV for 10 minutes.

**Cell-laden GelMA**

After printing, the glass vial was placed in a water bath at 37 °C for 5 min. In a biosafety cabinet at sterile conditions, a pre-warmed PBS was added to the vial to wash out the unpolymerized GelMA. The cell-laden constructs

were transferred to multi-well plates filled with cell medium and kept in the humidified CO<sub>2</sub> incubator at 37 °C for 6 days before the imaging session.

#### **Gel-SH / NB**

Once printing was complete, the vial was placed in an incubator at 37 °C for a few minutes to dissolve the uncrosslinked resin. The printed part was then gently washed in warm PBS, and then postcured for 30 s under UV.

#### **Confocal imaging of bioprinted constructs**

##### **Sample Preparation and Staining**

Printed hydrogel constructs were permeabilized with 0.1% Triton X-100 in PBS for 10 min at room temperature, followed by three washes of 5 min each with PBS.

To visualize cellular cytoskeletons, samples were incubated with Atto 488 (1:100 in PBS) for 30 min at room temperature, followed by three washes of 5 min each with PBS. Nuclei were stained with DAPI (1:1000 in PBS) for 5 minutes at room temperature, followed by a single PBS wash. All staining steps were performed in wet chambers protected from intense light.

##### **Confocal imaging**

Samples were imaged using a motorized inverted confocal microscope (Leica SP8). Sequential two-channel fluorescence acquisitions were performed to minimize spectral cross-talk: DAPI fluorescence was collected at 440–480 nm, and Atto 488 fluorescence was collected at 498–542 nm.

Three-dimensional image stacks (z-stacks) were acquired across the full thickness of the printed constructs with an axial step size of 10 μm. Image acquisition and microscope control were performed using LAS X software (Leica). Acquired images were processed and analyzed using Fiji/ImageJ.

##### **Micro-CT scans**

Millimeter-scale printed objects were imaged with voxel sizes of 3 × 3 × 3 μm<sup>3</sup> under a 160 kV X-ray transmission tomography (Hamamatsu, Japan). 3D visualizations and cross sections of the pieces were obtained using Fiji-ImageJ. centimeter-scale sample objects were imaged with voxel sizes of 20 × 20 × 20 μm<sup>3</sup>.

##### **Photography**

The printed parts were analyzed using a Keyence digital microscope (VHX-5000) with magnifications ranging from x20 to x200. The Human ear printed with norbornene was imaged using a FUJIFILM camera with an objective with a magnification ranging from x55 to x200, adapted with a MCEX-16 extension tube.

##### **Simulations**

3D renderings of STL files, along with recorded light intensities and simulated intensity distributions, were

generated using Wolfram Mathematica 14.2<sup>41</sup>. The tomographic projections were calculated through the Radon transform (Intensity targets for the holographic projections), as well as CGHs generation were calculated in MATLAB R2025a<sup>42</sup>.

#### **3D models**

The 3D Model of The Fusilli is custom-made. The DNA helix by linew on Thingiverse (<https://www.thingiverse.com/thing:3980700>) and The Stanford Bunny by printable (<https://www.printables.com/model/364039-stanford-bunny-fdm-printable/files>) are licensed under CC BY 4.0. The 3D model of the Human Ear by Faaxundo is licensed under CC BY-SA.

#### **Acknowledgements**

C.M. has received funding from the Eurostars-3 (VOLTA-EI3908) joint program with co-funding from the European Union's Horizon Europe research and innovation program, Innosuisse (Swiss Innovation Agency), and Innovation Fund Denmark (IFD). R.R. acknowledges grant application P5R5-3\_235066 from the Swiss National Science Foundation (SNSF). C.M. received funding from the Swiss National Science Foundation under project number 2000-1- 240074 10007068 "Neural precision holographic volumetric additive manufacturing". The authors would like to acknowledge Lionel Pittet, and Albert Taureg (PIXE Platform, EPFL) for their support with micro-CT imaging of the printed structures. The authors would like to acknowledge the Discovery Learning Labs (DLL) at EPFL for providing the imaging facilities, and especially thank Robin Amacher and Pierre-Etienne Bourban for their support with the use of the Keyence microscope.

#### **Author contributions**

M.I.A.C.: conceptualization, experiments, data acquisition, interpretation, and validation, simulations. Writing: original draft, reviewing, and editing. R.R.: Gel-SH / NB synthesis, sample preparation Gel-SH / NB, data curation, optical imaging. Writing: reviewing and editing. V.S. performed the cell laden GelMa sample preparation. Performed experiments and optical imaging. Writing: reviewing and editing. Y. P.: PLM control software development, co-supervision. Writing: original draft, reviewing, and editing. C.M.: conceptualization, methodology, supervision. Writing: original draft, reviewing, and editing.

#### **Data availability**

The data supporting the results of this study are available in the Supplementary Information.

#### **Code availability**

The code presented in this paper are available upon reasonable request.

#### **Conflict of interest**

C.M. is a shareholder of Readily3D (Switzerland), a company that develops and commercializes tomographic volumetric 3D printers. The authors declare no other conflicts of interest.

**Supplementary information** The online version contains supplementary material available at <https://doi.org/10.1038/s41377-026-02331-4>.

Received: 25 August 2025 Revised: 1 April 2026 Accepted: 22 April 2026  
Published online: 19 May 2026

#### **References**

- Bernal, P. N. et al. Volumetric Bioprinting of Complex Living-Tissue Constructs within Seconds. *Adv. Mater.* **31**, 1904209 (2019).

2. Jamróz, W. et al. 3D Printing in Pharmaceutical and Medical Applications – Recent Achievements and Challenges. *Pharm. Res.* **35**, 176 (2018).
3. Frazier, W. E. Metal Additive Manufacturing: A Review. *J. Mater. Eng. Perform.* **23**, 1917–1928 (2014).
4. Kodama, H. Automatic method for fabricating a three-dimensional plastic model with photo-hardening polymer. *Rev. Sci. Instrum.* **52**, 1770–1773 (1981).
5. Gibson, I., Rosen, D. & Stucker, B. *Additive Manufacturing Technologies: 3D Printing, Rapid Prototyping, and Direct Digital Manufacturing*. (New York: Springer, 2015), <https://doi.org/10.1007/978-1-4939-2113-3>.
6. Wang, X. et al. 3D printing of polymer matrix composites: A review and prospective. *Compos. Part B: Eng.* **110**, 442–458 (2017).
7. Bikas, H., Stavropoulos, P. & Chryssolouris, G. Additive manufacturing methods and modelling approaches: a critical review. *Int. J. Adv. Manuf. Technol.* **83**, 389–405 (2016).
8. Hahn, V. et al. Rapid Assembly of Small Materials Building Blocks (Voxels) into Large Functional 3D Metamaterials. *Adv. Funct. Mater.* **30**, 1907795 (2020).
9. Kelly, B. E. et al. Volumetric additive manufacturing via tomographic reconstruction. *Science* **363**, 1075–1079 (2019).
10. Loterie, D., Delrot, P. & Moser, C. High-resolution tomographic volumetric additive manufacturing. *Nature Commun.* **11**, 852 (2020).
11. Regehly, M. et al. Xolography for linear volumetric 3D printing. *Nature* **588**, 620–624 (2020).
12. Hahn, V. et al. Light-sheet 3D microprinting via two-colour two-step absorption. *Nat. Photonics* **16**, 784–791 (2022).
13. Álvarez-Castaño, M. I. et al. Holographic tomographic volumetric additive manufacturing. *Nature Commun.* **16**, 1551 (2025).
14. Ren, Y.-X., Lu, R.-D. & Gong, L. Tailoring light with a digital micromirror device. *ANNALEN DER PHYSIK* **527**, 447–470 (2015).
15. Correa-Rojas, N. A., Gallego-Ruiz, R. D. & Álvarez-Castaño, M. I. Generation of linearly polarized modes using a digital micromirror device and phase optimization. *Computer Opt.* **46**, 30 (2022).
16. Otón, J. et al. Multipoint phase calibration for improved compensation of inherent wavefront distortion in parallel aligned liquid crystal on silicon displays. *Appl. Opt.* **46**, 5667 (2007).
17. Haist, T. & Osten, W. Holography using pixelated spatial light modulators—part 1: theory and basic considerations. *J. Micro/Nanolithogr., MEMS, MOEMS* **14**, 041310 (2015).
18. Wu, P.-C., Yang, S.-Y. & Lee, W. Recovery of UV-degraded electrical properties of nematic liquid crystals doped with TiO<sub>2</sub> nanoparticles. *J. Mol. Liq.* **218**, 150–155 (2016).
19. Yang, Q. et al. Fast-Response Liquid Crystal Phase Modulators with an Excellent Photostability. *Crystals* **10**, 765 (2020).
20. Bartlett, T. A., McDonald, B. C. & Hall, J. Adapting Texas Instruments DLP technology to demonstrate a phase spatial light modulator. Proceedings of the SPIE 10932, Emerging Digital Micromirror Device Based Systems and Applications XI. San Francisco, California, United States: SPIE, 2019, 109320S, <https://doi.org/10.1117/12.2514483>.
21. Rocha, J. C. A. et al. Fast and light-efficient wavefront shaping with a MEMS phase-only light modulator. *Opt. Express* **32**, 43300–43314 (2024).
22. Kilcullen, P. et al. High-speed complex field modulation using binary phase-engraved superpixels. *Light: Adv. Manuf.* **6**, 17 (2025).
23. Fuentes, J. L. M. et al. Interferometric method for phase calibration in liquid crystal spatial light modulators using a self-generated diffraction-grating. *Opt. Express* **24**, 14159–14171 (2016).
24. Wechsler, F. et al. Wave optical model for tomographic volumetric additive manufacturing. *Opt. Express* **32**, 14705–14712 (2024).
25. Haist, T., Schönleber, M. & Tiziani, H. J. Computer-generated holograms from 3D-objects written on twisted-nematic liquid crystal displays. *Opt. Commun.* **140**, 299–308 (1997).
26. Madsen, A. G. & Glückstad, J. HoloTile: Rapid and speckle-suppressed digital holography by matched sub-hologram tiling and point spread function shaping. *Opt. Commun.* **525**, 128876 (2022).
27. Choi, S. et al. Time-multiplexed Neural Holography: A flexible framework for holographic near-eye displays with fast heavily-quantized spatial light modulators. Proceedings of the ACM SIGGRAPH 2022 Conference Proceedings. Vancouver, BC, Canada: Association for Computing Machinery (2022, 32).
28. Goodman, J. W. Some fundamental properties of speckle. *J. Optical Soc. Am.* **66**, 1145–1150 (1976).
29. Zhou, L. et al. Speckle-noise-reduction method of projecting interferometry fringes based on power spectrum density. *Appl. Opt.* **51**, 6974–6978 (2012).
30. Restrepo, J., Correa-Rojas, N. & Herrera-Ramírez, J. Speckle Noise Reduction in Digital Holography Using a DMD and Multi-Hologram Resampling. *Appl. Sci.* **10**, 8277 (2020).
31. Sgarminato, V. et al. 3D in vitro modeling of the exocrine pancreatic unit using tomographic volumetric bioprinting. *Biofabrication* **16**, 045034 (2024).
32. Boniface, A. et al. Volumetric helical additive manufacturing. *Light: Adv. Manuf.* **4**, 124–132 (2023).
33. Webber, D. et al. Micro-optics fabrication using blurred tomography. *Optica* **11**, 665–672 (2024).
34. Zhang, Y. J. et al. Advancing Tomographic Volumetric Printing Via Oxygen Inhibition Control: Improved Accuracy and Large-Volume Capability. *Adv. Mater.* **37**, e08729. <https://doi.org/10.1002/adma.202508729> (2025).
35. Peng, Y. et al. Neural holography with camera-in-the-loop training. *ACM Trans. Graph.* **39**, 185 (2020).
36. Campos, J. et al. Characterization of the Liquid Crystal Display Modulation. Optimization for Some Applications. *Acta Phys. Polonica* **101**, 189–200 (2002).
37. Ambs, P. & Bigue, L. Characterization of an analog ferroelectric spatial light modulator: application to dynamic diffractive optical elements and optical information processing. Proceedings of the SPIE 10302, Optoelectronic Information Processing: Optics for Information Systems: A Critical Review. Valencia, Spain: SPIE, 2001,103020I, <https://doi.org/10.1117/12.449680>.
38. Macfaden, A. J. & Wilkinson, T. D. Characterization, design, and optimization of a two-pass twisted nematic liquid crystal spatial light modulator system for arbitrary complex modulation. *J. Optical Soc. Am.* **34**, 161–170 (2017).
39. Van Den Bulcke, A. I. et al. Structural and Rheological Properties of Methacrylamide Modified Gelatin Hydrogels. *Biomacromolecules* **1**, 31–38 (2000).
40. Rizzo, R. et al. Multiscale Hybrid Fabrication: Volumetric Printing Meets Two-Photon Ablation. *Adv. Mater. Technol.* **8**, 2201871 (2023).
41. Wolfram Research, Inc. Mathematica. (Wolfram Research, Inc, 2024).
42. The MathWorks Inc. MATLAB version: 25x (R2025a). (2025).